ELSEVIER

Contents lists available at ScienceDirect

Ceramics International

journal homepage: www.elsevier.com/locate/ceramint



Microstructure and friction coefficient of ceramic (TiC, TiN and B₄C) reinforced Ni-based coating by laser cladding



Yu Zhao^{a,b,**}, Tianbiao Yu^{a,b,*}, Chuang Guan^{a,b}, Jiayu Sun^c, Xuefei Tan^{a,b}

- ^a School of Mechanical Engineering and Automation, Northeastern University, Shenyang, 110819, China
- b Liaoning Provincial Key Laboratory of High-end Equipment Intelligent Design and Manufacturing Technology, Northeastern University, Shenyang, 110819, China
- ^c Deformation Processing Institute for Materials Research, Tohoku University, Sendai, 980-8577, Japan

ARTICLE INFO

Keywords: Laser cladding B₄C/TiC/TiN ceramic coating Microstructure Microhardness Friction coefficient

ABSTRACT

Ni204 ceramic composite coatings with different mass fractions of TiC, TiN and B4C were successfully prepared on the surface of 45 steel by laser cladding. Microstructures of different ceramic coatings were studied using X-ray diffraction, scanning electron microscopy and laser confocal microscopy. The friction coefficient and microhardness of ceramic coatings were measured with a reciprocating friction wear machine and microhardness tester. The results show that ceramic coating has $766.8 \text{HV}_{0.5}$ average microhardness and friction coefficient of 0.47 when 10%TiC, TiN, and $B_4\text{C}$ are added to initial powder Ni204. The microstructure of cladding layer is uniform and compact, and the microhardness and friction coefficient of the coating increased and decreased by factors 2.6 and 1.393 compared with initial powder. This is due to the presence of multiple phase ((Ti, Mo, Nb) (C, B, N)), carbide, nitride, (Ti, Mo, Nb) (C, B, N), and (Ti, Mo, Nb) (C, N) ring phase around TiC, TiN, and Ti(C, N) ceramic phases. Uniformly distributed reinforced phases in the coating inhibit extrusion by grinding balls on the surface of the ceramic coating, thus changing original abrasive wear mechanism, making wear marks more shallow, and decreasing friction coefficient of the surface.

1. Introduction

Machine tool parts (such as gears, spindles) are mainly made of steel. After processing, the parts must undergo post-processing (e.g., normalizing, tempering, carburizing, or nitriding) to provide high hardness, low friction coefficient, and strong corrosion resistance. With the development of rapid prototyping technology, high performance materials coated on the surface of parts are widely used for surface modification and strengthening [1-3]. At present, coatings prepared vie thermal spraying contain pores and exhibit poor interlayer metallurgical bonding [4]. The coating prepared by self-propagating synthesis is affected by material properties and the shape of the workpiece [5]. There is interlayer interface [6] in powder metallurgy. Chemical vapor deposition must be performed at high temperature and high pressure, causing the workpiece to deform [7]. It is difficult to control the composition of the coating with physical vapor deposition [8]. However, laser cladding technology can be used to produce functional surfaces on the surface of parts with lower costs and higher efficiency [9,10].

The wettability of an Ni-based alloy and machine tool parts (steel parts) is high, and there are few pores and cracks on the interface. The ceramic phase in an Ni-based coating has a good bonding performance in the coating, and including ceramic particles can significantly decrease the friction coefficient and hardness of the Ni-based coating [11]. However, producing a pure ceramic coating is difficult due to crack formation at the interface during the cladding process. Therefore, composite powders of ceramics and alloys are usually prepared to improve the surface properties of the samples. Ma et al. [8] studied the effect of Ti on the microstructure and the microhardness of Ni60/WC composite coatings. Ti limits the growth of Cr₅B₃ ceramics and in situ synthesized TiC ceramic phases promote decomposition of WC. After the addition of Ti, the microhardness of the coating decreased slightly, but the friction coefficient increased by a factor 2.6 compared to the initial coating. Li et al. [12] in situ synthesized TiB2 and TiC ceramic phases by laser cladding Al₂O₃/TiO₂/B₄C/Al composite powder with a CO₂ laser, yielding an Al₂O₃/TiB₂/TiC composite ceramic coating. Within a certain mass fraction, the increased Al₂O₃ content decreases the hardness of the composite coating but increases the friction

^{*} Corresponding author. School of Mechanical Engineering and Automation, Northeastern University, Shenyang, 110819, China.

^{**} Corresponding author. School of Mechanical Engineering and Automation, Northeastern University, Shenyang, 110819, China. E-mail addresses: zhaoyuneu@gmail.com (Y. Zhao), tianbiaoyudyx@gmail.com (T. Yu), guanchuang10193@163.com (C. Guan), sunjiayudewo@gmail.com (J. Sun), tanxf@me.neu.edu.cn (X. Tan).

Table 1 Chemical composition of the substrate and Ni204 powder (wt. %).

	С	P,S	Si	Cr	Ni	Mn	Mo	Nb	Cu	Fe
Ni204	≤0.03	-	0.4	21	Bal.	-	9	4 –	-	1.5
45 steel	0.42–0.5	≤0.045	0.17–0.37	≤0.25	≤0.25	0.5-0.8	-		≤0.25	Bal.

coefficient. Fomin et al. [13] found that the number of pores and cracks in the B_4 C/Ni composite coating prepared with laser cladding was less than that prepared with cold spraying, and the ceramic phase was more evenly distributed in the coating, where the size decreased by a factor 2 to 3. Li et al. [14] prepared Ti/TiBCN composite coatings with different TiBCN content using laser cladding. The hardness of TiBCN is higher than the matrix. More TiBCN precipitates and becomes evenly distributed in the coating during cladding as the TiBCN content increases, which refines the microstructure of the coating, thus increasing the microhardness, corrosion resistance, and wear resistance of the composite coating.

Composite or ceramic phases in the composite coating prepared with B₄C, TiC, TiN, TiB₂, and viscous metals can effectively increase the microhardness and wear resistance. These materials are often used to decrease the friction coefficient, as well as increase the hardness of mechanical parts and the corrosion resistance of metallurgical mineral parts [7,11,15]. B₄C, TiC, and TiN are ceramic particles with high melting point, high hardness, and stable chemical properties. TiC and TiN have similar thermal expansion coefficients and good compatibility. Therefore, they serve as enhancers to produce multiple reinforcement phases in the microstructure simultaneously. During laser cladding, B₄C usually forms a cementite of M₃C, M₇C₃, and M₂₃C₆ with Fe and Cr (e.g., M = Cr and Fe, or C=B and C) [16]. Larger ceramic particles were clustered around the NiAl phase in the coating formed via direct addition of TiC-TiB2 compared to the in-situ synthesized TiC-TiB₂ multiphase ceramic [5]. The wear resistance in composites with the TiC-TiB₂ phase are stronger than those in the individual TiC, or TiB2 phases [17,18]. In-situ synthesis of the ceramic phase in the coating provides more advantages. Jiang et al. [19] prepared Ni-B4C composite coatings with different B₄C contents by electro deposition, and it was found that the microhardness of composite coating were positively correlated with B₄C content. 6 g/L of B₄C in the bath yielded a coating with the highest corrosion resistance. Wang et al. [18] in-situ synthesized TiB and TiC from Ti, B₄C, and C, and its influence on composite coating superplastic was studied. The largest elongation was found to be 659% when 5% of the reinforced phase was generated in the coating. When the weight fraction of the reinforcing phase exceeded 5%, the elongation decreased as the ceramic phase size increased. Wu et al. [9] studied the effect of Mo on the microstructure and wear properties of in situ synthesized Ti(C, N)/Ni-based composite coatings. The results show that the (Ti, Mo) (C, N) ring phase appears at the edge of Ti(C, N), and Mo decreases the grain size, which increases the microhardness and wear resistance of the coating. Yeh et al. [20] added Ti + B₄C and Ti + BN to an Ni-Al combustion system to in situ synthesize TiB₂+TiC and TiB₂+TiN ceramic phases, respectively. It was found that Ti + B₄C had low reaction activation energy, good phase transition performance, and high fracture toughness. TiB2-B4C multiphase ceramics have good sintering properties, high melting point, and low diffusion coefficient, and have the properties of TiB2 and B4C single-phase ceramics [11,20].

Many research teams prepared TiC/B₄C/TiN composites by sintering [6,11], high-temperature synthesis [5] and spraying [4,7], yet the use of laser cladding to fabricate the composites is less common. Even fewer studies have focused on preparing a TiC/B₄C/TiN/Ni204-based composite using laser cladding. In this study, Ni204 alloy powder was selected as the initial powder, and B₄C, TiC and TiN powder were used as additive materials. Different mass fractions of (TiC, B₄C, TiN)/Ni204-based composite coatings were fabricated by laser cladding. The

microstructure, elemental distribution, phase composition, and morphology of the $B_4C/TiC/TiN/Ni204$ composite ceramic coatings were investigated. The mechanism determining the microhardness and friction coefficient in the $B_4C/TiC/TiN/Ni204$ coating was investigated.

2. Experimental

2.1. Coating and substrate materials

 $100\times100\times10~\text{mm}^3$ 45 steel was used as a substrate. Its chemical composition and the chemical composition of the initial Ni204 powder are listed in Table 1. The substrate was sanded with sand paper, cleaned with alcohol, and then dried before deposition.

The composite ceramic powders used in laser cladding contained $B_4 C$ (99.9% purity, 2–3 $\mu m)$, TiC (99% purity, 6–10 $\mu m)$, TiN (99.5% purity, 2–10 $\mu m)$ ceramic particles, and Ni204-based powders (53–150 $\mu m)$, and the proportions of each precursor used to fabricate various samples are shown in Table 2. Fig. 1 shows SEM images of the ceramics and a 10%TiC/10%TiN/10%B_4C/70%Ni204 composite. The ceramic powder and Ni204 powder were dried in a drying oven at 120 °C for 6 h before weighing. The powders were mixed with a ball mill machine at 30 rpm for 2 h, and the weight ratio of ceramic balls to powder was 2:1. The powders were uniformly mixed and dried in an oven at 120 °C for 4 h.

2.2. Laser cladding equipment

A YLP-500 continuous output IPG fiber laser was used for laser cladding. The off-line programming software is used to obtain the robot code to control the KUKA robot, and then the composite coating which runs according to the designed trajectory is obtained, as shown in Fig. 2(a). During the experiment, the scanning speed is preset in the robot code, the powder feeding speed and feed gas flow rate were regulated with a single barrel powder feeder (RC-PGF-1). The laser power was regulated with the control cabinet of the assembled laser cladding system [21]. Ar was used as the shielding gas and carrier gas during the experiment.

2.3. Composite coating fabrication and laser cladding process parameters

The Ni-based powders were placed into a powder feeding bucket in the laser cladding system. The laser beam was moved along the same to fabricate the composite coating. The cross-sectional morphology of the composite coating is shown in Fig. 2(b).

During laser cladding, an excessive flow of shielding gas would blow the powder bundle away from the beam, but the powder would oxidize if the shielding gas flow was too low. Therefore, the shielding gas flow was set to $15\,\mathrm{L/min}$ during laser cladding. The beam waist on the powder would also be too large due to poor focusing if the carrier gas

 Table 2

 Ceramic composite powder content used to fabricate each sample.

Ingredient (wt. %)	TiC	TiN	B ₄ C	Ni204
Sample 1	10	10	10	70
Sample 2	15	15	0	70
Sample 3	0	0	0	100
Sample 4	2.5	2.5	10	85

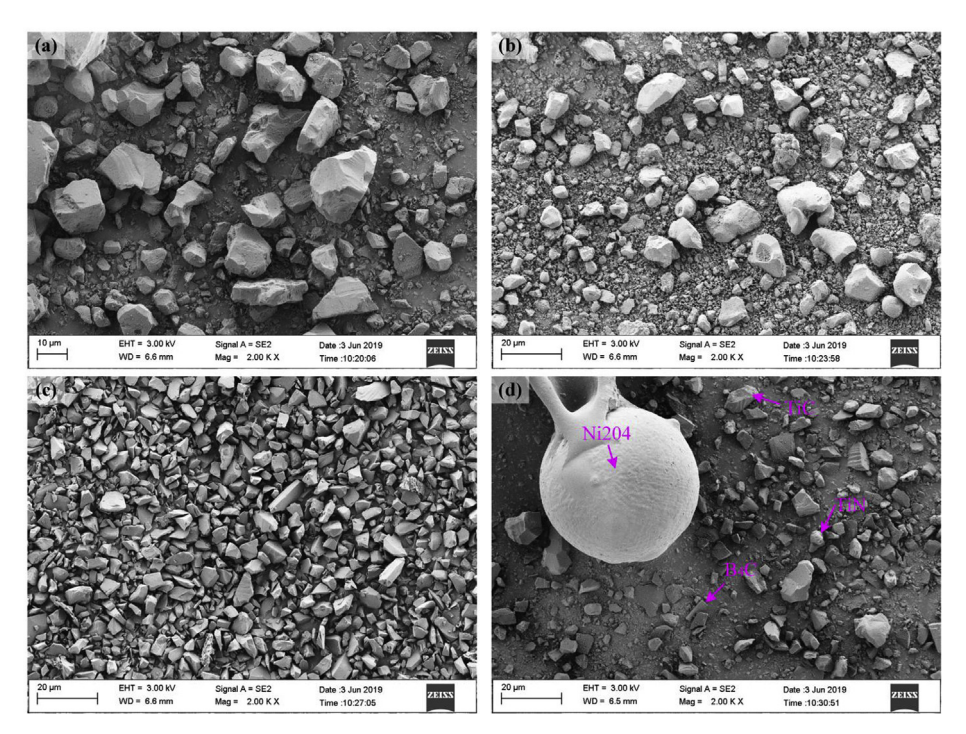


Fig. 1. SEM images of ceramic particles and the composite powder. (a) TiC; (b) TiN; (c) B₄C; (d) 10%TiC/10%TiN/10%B₄C/70%Ni204.

flow rate was too low, resulting in a thin cladding. However, powder particles would pass through the beam for a short time and absorb less energy if the carrier gas flow rate was too large, yielding an incomplete cladding. Therefore, the carrier gas flow rate during the cladding process was set to 8 L/min. The beam was focused directly on the powder during cladding, i.e., cladding was conducted in the focal plane. During the early stage, the laser cladding process parameters were optimized in order to prevent crack and pore formation. During the experiment, the laser power was set to 450 W and focused to 1.1 mm diameter. The scanning speed was set to 5.5 mm/s, the powder feeding disc was rotated at 0.7 rpm, and the Ni204 powder mass flow rate was 11.056 g/min. Adjacent tracks were spaced 0.85 mm apart with 35% lateral overlap. The sample was translated along the z-axis by 0.35 mm and the longitudinal overlap rate was 23.9%.

2.4. Composite coating properties

After laser cladding, metallographic and X-ray diffraction (XRD) specimens were prepared by wire cutting as shown in Fig. 2(c). After polishing, metallographic specimens were etched with HCl:HNO $_3$:H $_2$ O = 2:1:1 (volume) etching solution. XRD specimens were cut into $10 \times 5 \text{ mm}^2$ rectangles. Laser confocal microscopy (OLYMPUS LEXTOLS4100) was used to observe the macro-morphology of the coating cross section. The phase distribution in the ceramic composite was examined with an X-ray diffractometer (XRD, X

Pertpro). The microstructure, phase morphology, elemental distribution, and energy spectrum analysis of the composite coating were measured with a field emission scanning electron microscope (SEM, Zeiss Ultra Plus).

The microhardness distribution along the depth cross section of the ceramic Ni-based composite coatings was measured with a microhardness tester (EM500-2A). A 500 gf load was applied for $12 \, \text{s}$, and the indentation morphology was measured with an optical microscope that was equipped with the microhardness tester. A reciprocating friction wear tester (MFT-4000) was used to measure the friction coefficient of ceramic Ni-based composite coatings. Dry friction on the surface of the coatings studied at room temperature. A $1 \, \text{kg}$ weight was used for loading during wear testing. The reciprocating distance, speed, and time were set to $5 \, \text{mm}$, $200 \, \text{mm/min}$, and $30 \, \text{min}$. A $2 \, \text{rO}_2$ ceramic ball with $5 \, \text{mm}$ diameter (HRC > 90) was used for grinding. 2D and 3D wear morphologies of the composite coatings were observed with the laser confocal microscope.

3. Results

3.1. Analysis of phase and microstructure of the composite coating

3.1.1. Coating phase analysis

X-ray diffraction patterns of ceramic Ni-based composite coatings and ceramic powders are shown in Fig. 3. Fig. 3(a) shows XRD

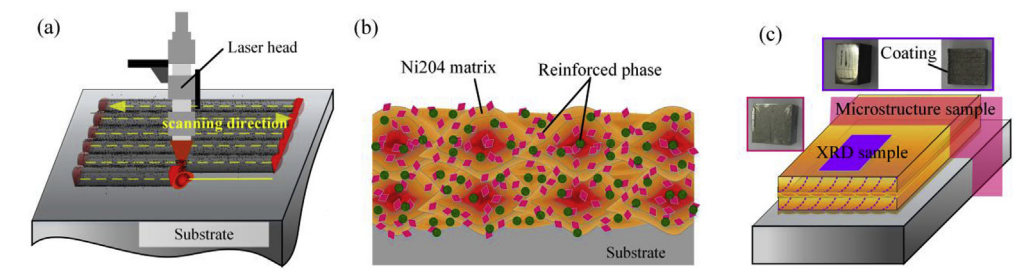


Fig. 2. Experimental diagram and sample preparation procedure. (a) Coating pattern generation; (b) Schematic diagram showing the cross section of the morphology; (c) Sample preparation.

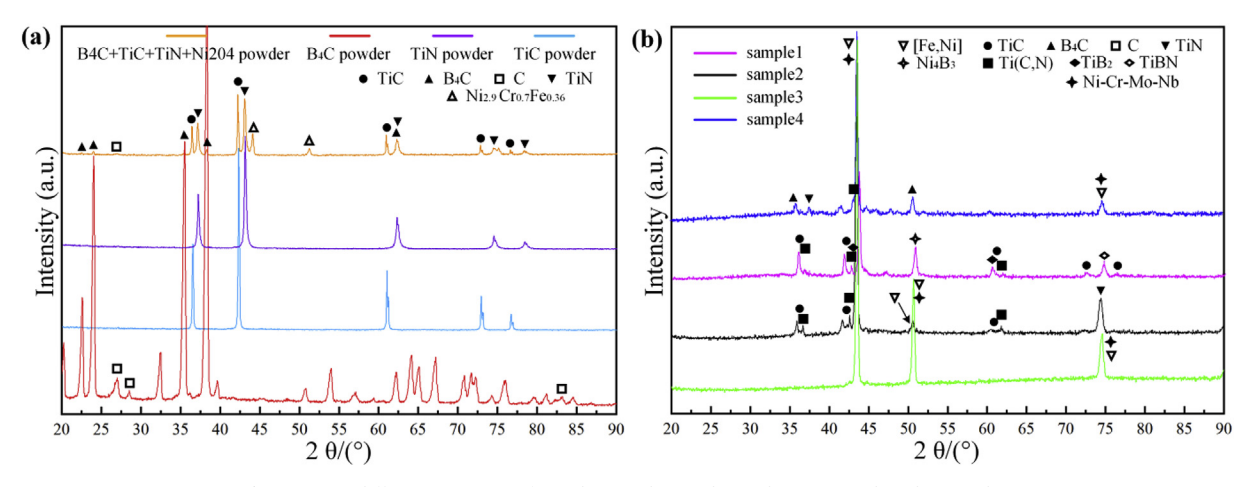


Fig. 3. X-ray diffraction patterns from the powders and samples. (a) Powder; (b) Samples.

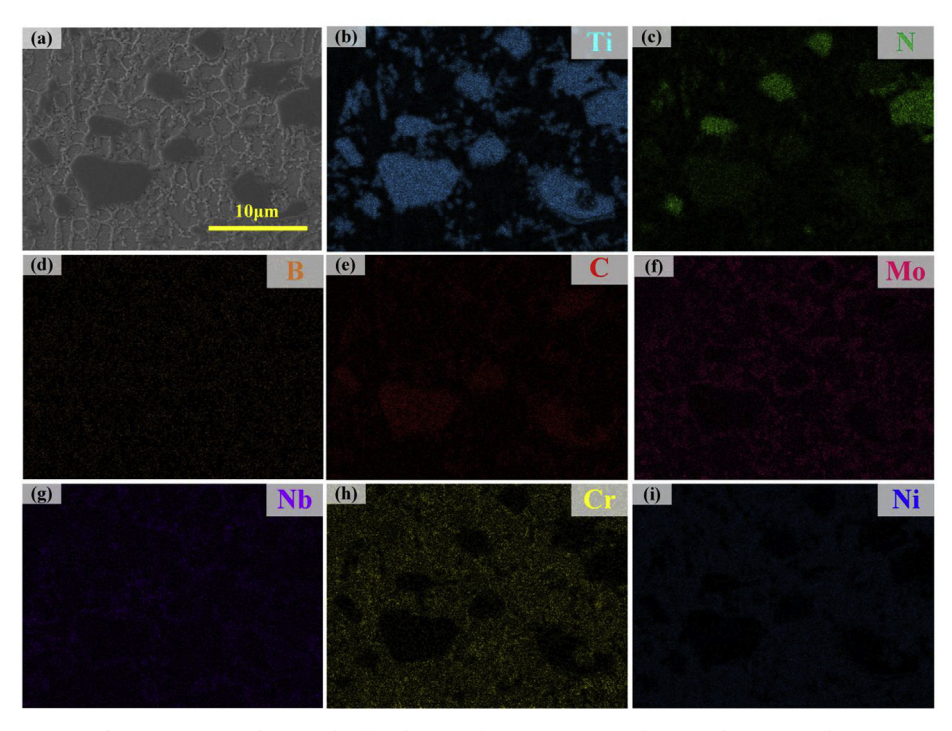


Fig. 4. EDS maps showing the distribution of N, C, B, Ti, Mo, Nb, Cr, and Ni in sample 1.

diffraction peaks corresponding to TiC, TiN, B₄C, and the TiC/TiN/B₄C/Ni204 composite. All ceramic phases are detected in the composite powder and all elements in the Ni204 alloy powders exist as compounds or solid solutions. Fig. 3(b) shows XRD diffraction peaks from samples 1–4. The main phases in sample 3 were Ni–Cr–Nb–Mo and [Fe, Ni]. When 15%TiC and 15%TiN were added to Ni204, the main phases in sample 2 were TiC, TiN, Ti(C, N), [Ni, Fe], and Ni–Cr–Nb–Mo. When 10%TiC, 10%TiN and 10%B₄C were added to Ni204, the main phases in the sample 1 coating are TiC, TiN, Ti(C, N), Ni₄B₃, TiB₂, [Ni, Fe], and Ni–Cr–Nb–Mo. When 2.5%TiC, 2.5%TiN and 10%B₄C were added to Ni204, the main phases in sample 4 were TiC, TiN, Ti(C, N), B₄C, [Ni, Fe], and Ni–Cr–Nb–Mo. Aside from TiC, TiN and B₄C, new phases were detected in samples 1, 2, and 4, indicating the following reaction occurred between ceramic particles and the Ni204 alloy powder during laser cladding [6,21,22]:

$$xTiC + (1-x)TiN = Ti(C_X, N_{1-X})$$
(1)

$$16Ni + 3B_4C = 4Ni_4B_3 + 3C (2)$$

$$2TiC + B_4C = 2TiB_2 + 3C \tag{3}$$

Due to the similar lattice structure of TiC and TiN, they easily form a Ti(C, N) solid solution. When the cladding temperature is higher than 1200 K, the Gibbs free energy is negative, indicating reaction (1) can proceed spontaneously. When x in Ti(C_x, N_{1-x}) decreases, the absolute value of the Gibbs free energy increases, thus Ti(C_{0.2}, N_{0.8}) is the more stable [21] compared with x = 0.3 and 0.7. When the temperature is higher than 1273.15 K, B₄C diffuses into Ni and reaction (2) proceed spontaneously [6]. Therefore Ni₄B₃ was produced in the reaction between Ni and B₄C, but the corresponding C content increased [6]. Carbides formed from the reaction between C, Fe, Mo, Cr, and Nb [9,16]. According to thermochemical data on a B₄C–TiC system [23], the Gibbs free energy in (1) was $-201.800\,\text{kJ/mol}$ at 2100 K [24]. Therefore reaction (1) could occur during laser cladding, forming TiB₂. TiC, TiN and B₄C was still detected in the samples, indicating that the reactions were incomplete.

3.1.2. Coating composition analysis

Fig. 4 shows the surface distribution of Ti, N, C, B, Mo, Nb, Cr and Ni

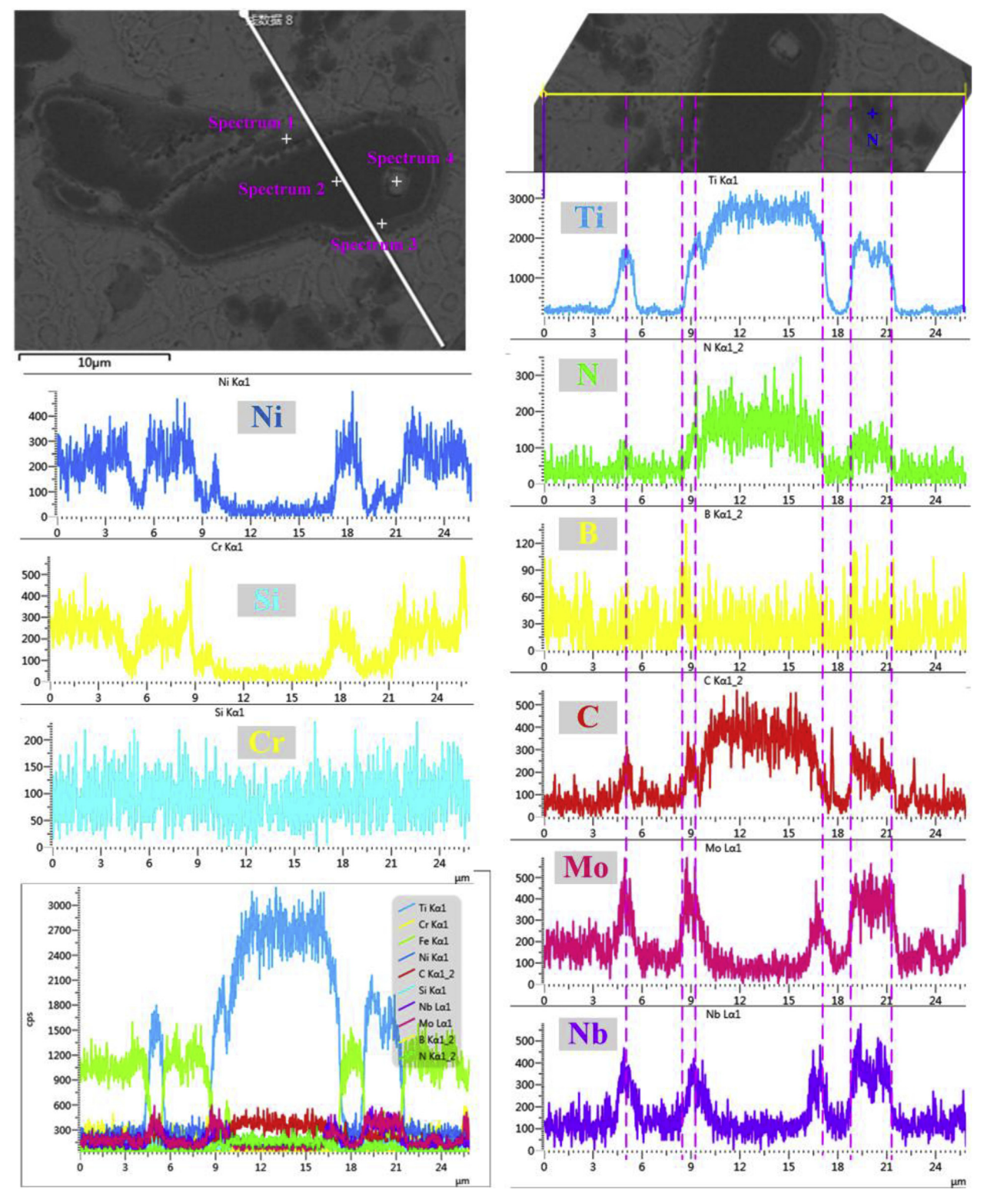


Fig. 5. EDS line scan results of N, C, B, Ti, Mo, Nb, Cr, and Ni in sample 1.

elements in sample 1. According to the EDS mapping results, the gray-black phases in Fig. 4(a) primarily contain Ti, N, and C. Combining with the XRD results (Fig. 3), one finds that the TiN, TiC, and Ti(C, N) ceramic phases formed in this sample. Fig. 4(d) shows that B is dispersed in the coating. According to Fig. 4(b)-(c), (e)-(g), Ti, C, N, Mo, and Nb were simultaneously detected around the gray-white edge phase, indicating formation of multiphase (Ti, Mo, Nb) (C, N) [9,25,26]. The existence of Mo and Nb plays a role in solid solution

strengthening, and it increases the wettability of the ceramic phase and matrix [27]. The primary elements in the crystal are Ni and Cr, while the main elements along the grain boundary are Ni, Cr, Mo, and Nb. Mo can hinder coarsening of carbides [28], and affects diffusion of Ti, Nb, C and B in liquids [29]. When B_4C was added, the concentration of N, B, and C in the melt increases, while Ti, Nb, C, and B initially form (Ti, Nb) (B, C, N). Mo then begins to gather around (Ti, Nb) (C, B, N), forming the (Ti, Mo, Nb) (C, B, N)ring phase [28].

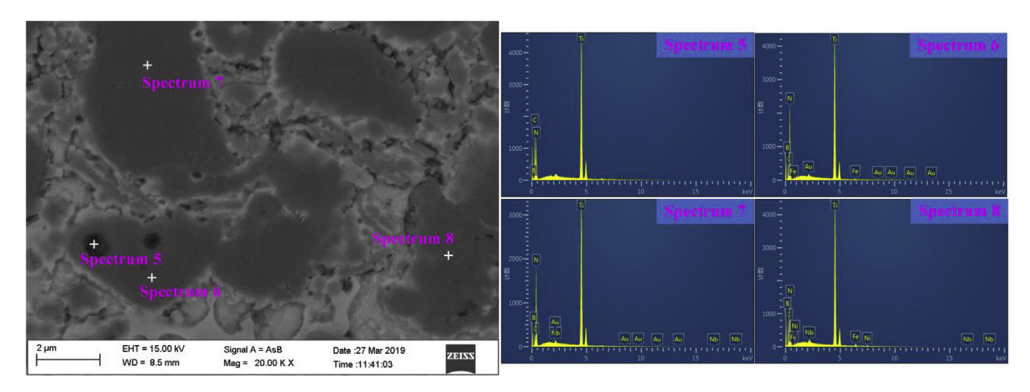


Fig. 6. EDS spectra obtained from sample 1.

Table 3 EDS spectra analyses results of sample 1 (in wt. % and at. %).

Marked locations		Ti	N	С	В	Nb	Мо	Ni	Cr	Fe
Spectrum 1	wt.%	42.10	4.42	20.34	0.0	5.06	6.07	3.02	4.40	14.58
	at.%	25.82	9.28	49.77	0.0	1.60	1.86	1.51	2.48	7.67
Spectrum 2	wt.%	76.39	0.0	22.05	0.0	0.53	0.0	0.53	_	0.85
	at.%	46.16	0.0	53.15	0.0	0.16	0.0	0.16	-	0.44
Spectrum 3	wt.%	70.08	0.0	18.85	0.0	6.31	2.84	0.54	-	1.37
_	at.%	46.24	0.0	49.61	0.0	2.15	0.94	0.29	-	0.77
Spectrum 4	wt.%	14.4	0.0	6.47	0.0	1.0	0.79	19.32	4.98	52.68
-	at.%	13.42	0.0	24.06	0.0	0.48	0.37	14.69	4.27	42.12
Spectrum 5	wt.%	61.60	15.51	18.84	4.05					
_	at.%	29.65	25.53	36.17	8.65					
Spectrum 6	wt.%	68.90	22.11	5.49	1.62					0.79
•	at.%	39.48	43.33	12.54	4.11					0.39
Spectrum 7	wt.%	67.02	22.59	5.07	4.16	0.02				
•	at.%	36.58	42.16	11.03	10.07	0.01				
Spectrum 8	wt.%	65.60	14.79	11.06	4.50	0.87		1.14		2.05
•	at.%	35.77	27.59	24.05	10.88	0.24		0.51		0.96

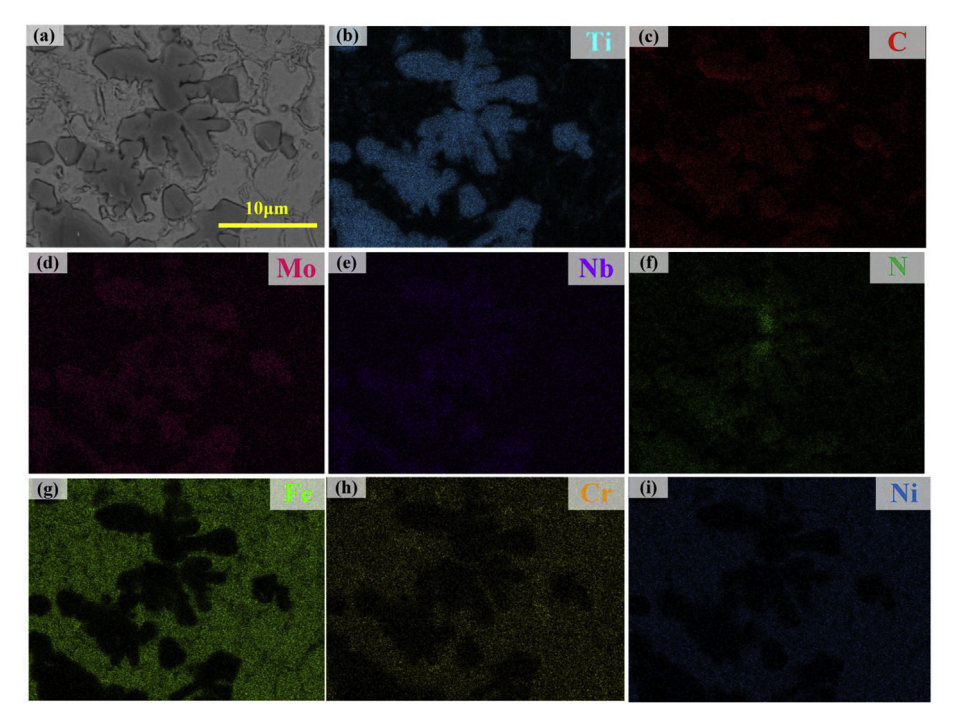


Fig. 7. EDS maps of N, C, Ti, Mo, Nb, Cr, Ni, and Fe in sample 2.

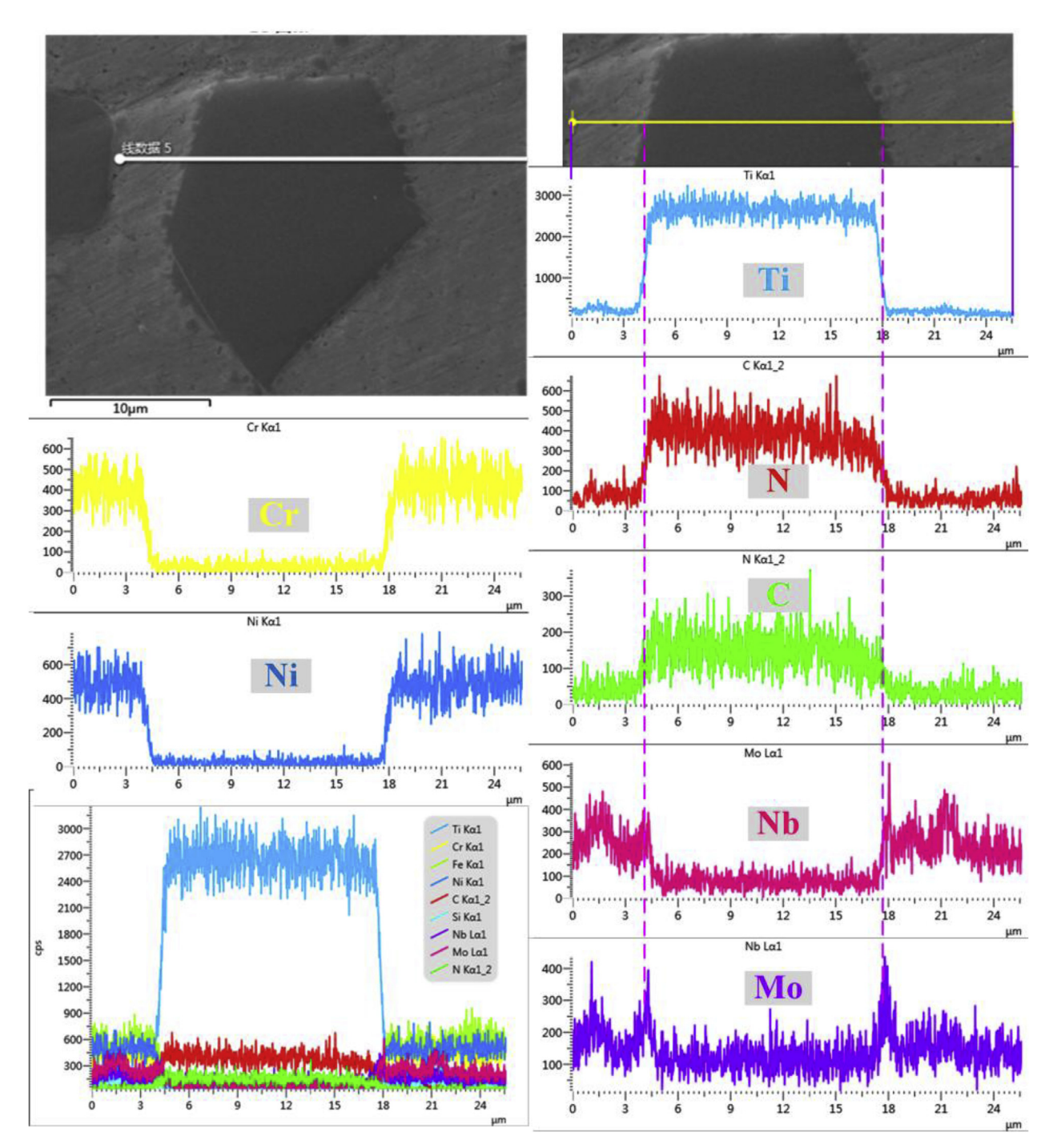


Fig. 8. EDS line scan results of the pentagonal phase in sample 2.

Fig. 5 shows the distribution of Ti, N, B, C, Mo, Nb, Ni, Cr, and other elements in the ceramic phase (ellipse) and matrix. The elliptical ceramic phase has good wettability with the matrix. Milky white and light gray ring phases appear around the ceramic phase. EDS line scan results show that the larger gray-black ceramics primarily contain Ti, N, and C, indicating formation of the Ti(C, N) ceramic phase. Ti, Mo, Nb, and Ni were detected in the milky white ring phase, which may be a solid solution of Ti–Mo–Nb–Ni. The light gray ring phase are primarily contains Ti, N, B, C, Mo, and Nb, indicating the formation of multiphase (Ti, Nb, Mo) (C, N, B) [9,25,26]. Area N primarily contains Ti, N, C, Mo, and Nb, while B diffused the interior. No ring phase formed in region N. During laser cladding, Ti, Nb, C, and B form a solid solution of (Nb, Ti)C and (Nb, Ti)B [30], while TiC and TiN particles form the Ti(C, N) phase.

Mo forms multiphase (Ti, Nb, Mo) (C, N, B) with (Nb, Ti)C, (Nb, Ti)B and Ti(C, N) phases [9,29].

The ceramic and ring phases in spectra 1–4 in Fig. 5 and spectra 5–8 in Fig. 6 were further analyzed. EDS spectroscopic analysis of elemental content at points 1–8 is shown in Table 3. The XRD results in Fig. 3 show that the gray-black phase is TiC, TiN and Ti(C, N) [9,21] ceramic phases. The ring phase around the gray-black ceramic phase is (Ti, Nb, Mo) (C, N). Energy spectra 6–8 region indicate the presence of Ti, B, C, and N, and the phases in this region are multiphase (Ti, B, N, C) ceramics. The black region (energy spectrum 5) may be a carbide produced from the reaction between $B_4 C$ and the composite.

The surface distribution of Ti, C, N, Mo, Nb, Cr, Fe, and Ni in sample 2 is shown in Fig. 7. Fig. 7(b)-(f) shows that Ti, C, N, Mo, and Nb are the

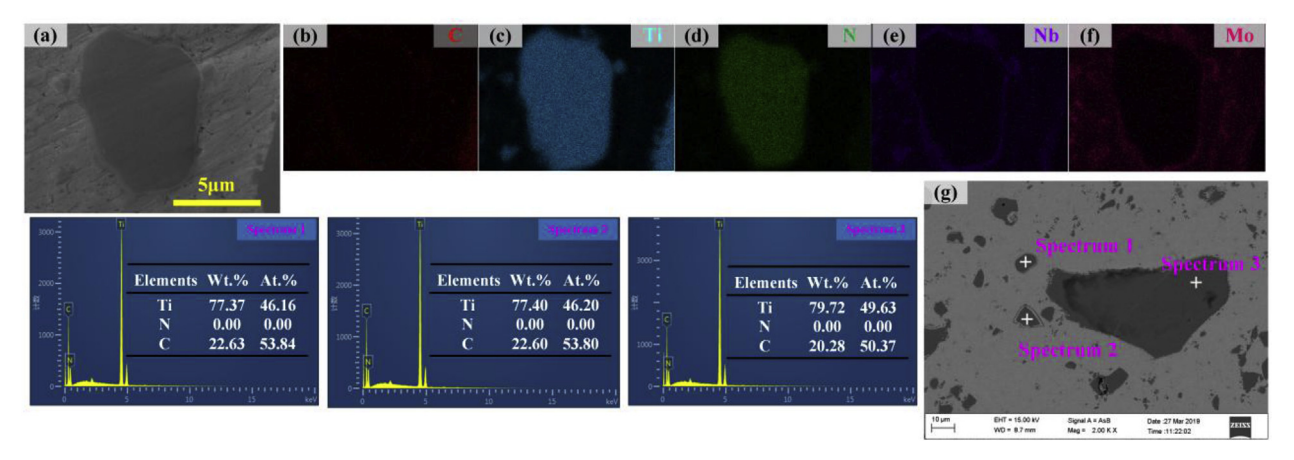


Fig. 9. EDS mapping analysis results and spectra obtained from sample 2.

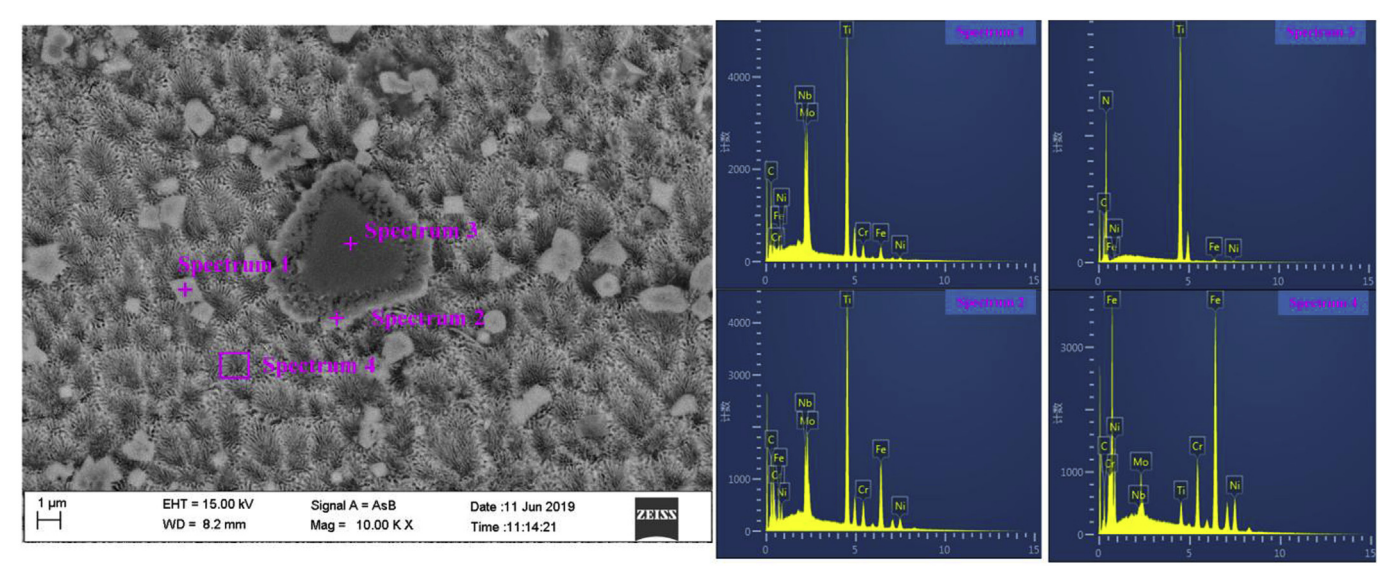


Fig. 10. EDS line scan and spectra from sample 4.

Table 4
Elemental content in sample 4 (in wt. % and at. %).

Marked locations		Ti	N	С	В	Nb	Мо	Ni	Cr	Fe
Spectrum 1	wt.%	42.11	0	20.02	0	15.35	12.33	1.34	3.71	5.15
	at.%	29.05	0	55.09	0	5.46	4.25	0.75	2.36	3.05
Spectrum 2	wt.%	33.85	0	14.76	0	8.65	7.96	6.03	5.49	23.26
	at.%	25.82	0	44.90	0	3.40	3.03	3.75	3.86	15.22
Spectrum 3	wt.%	63.28	25.82	9.10	0	0	0	0.46	0	1.34
	at.%	33.41	46.62	19.17	0	0	0	0.2	0.61	0.61
Spectrum 4	wt.%	2.66	0	8.47	0	0.94	4.57	15.58	10.50	57.28
	at.%	2.40	0	30.50	0	0.44	2.06	11.48	8.74	44.38

primary elements in the enhanced phase. Combined with the XRD results, one can see that the enhancement phase in Fig. 7(a) is Ti (C, N), and Mo and Nb dissolve in the Ti(C, N) phase to form (Ti, Mo, Nb) (N, C) [9,25,26]. The composition of the reinforcement phase in sample 2 is obviously different from that in sample 1. TiN and TiC in the composite coating mainly exists as Ti(C, N), while Nb diffuses into Ti(C, N)to form (Ti, Nb) (C, N) solid solution [30] with Nb in the cladding layer. Mo can also diffuse into Ti(C, N) [9], forming a multiphase with Mo [28]. Therefore, Nb, Mo and Ti (C, N) exist as multiphase (Ti, Mo, Nb) (N, C) rather than forming ring phases around the Ti (C, N) phase. The addition of B₄C causes Mo and Nb dissolved in the large Ti(C, N) ceramic phase to diffuse to the edge and form a (Ti, Mo, Nb) (C, B, N) ring phase around Ti(C, N) ceramic phase.

Fig. 8 shows the distribution of Ti, N, C, Mo, Nb, Ni, Cr and other elements along the gray-black reinforcement phase (polygon) and matrix in sample 2. The elements in the reinforced phase are Ti, N and C. According to the XRD test results, one can see that the polygonal reinforced phase is Ti(C, N). There is no ring phase around the Ti(C, N) ceramic phase, and the elemental content of Ti, N and C at the edge of the Ti(C, N) ceramic phase suddenly decreases. Mo and Nb do not form a shell-core structure around the Ti(C, N) ceramic phase. While the small grain size phase appeared in the periphery of the Ti(C, N) ceramic phase. According to the results of line scan, it can be determined that it is mainly composed of Mo and Nb elements.

Fig. 9(b)-(f) shows EDS maps from the TiN ceramics (ellipse). Results from the ceramic phase in Fig. 9(a) show that the light gray-black

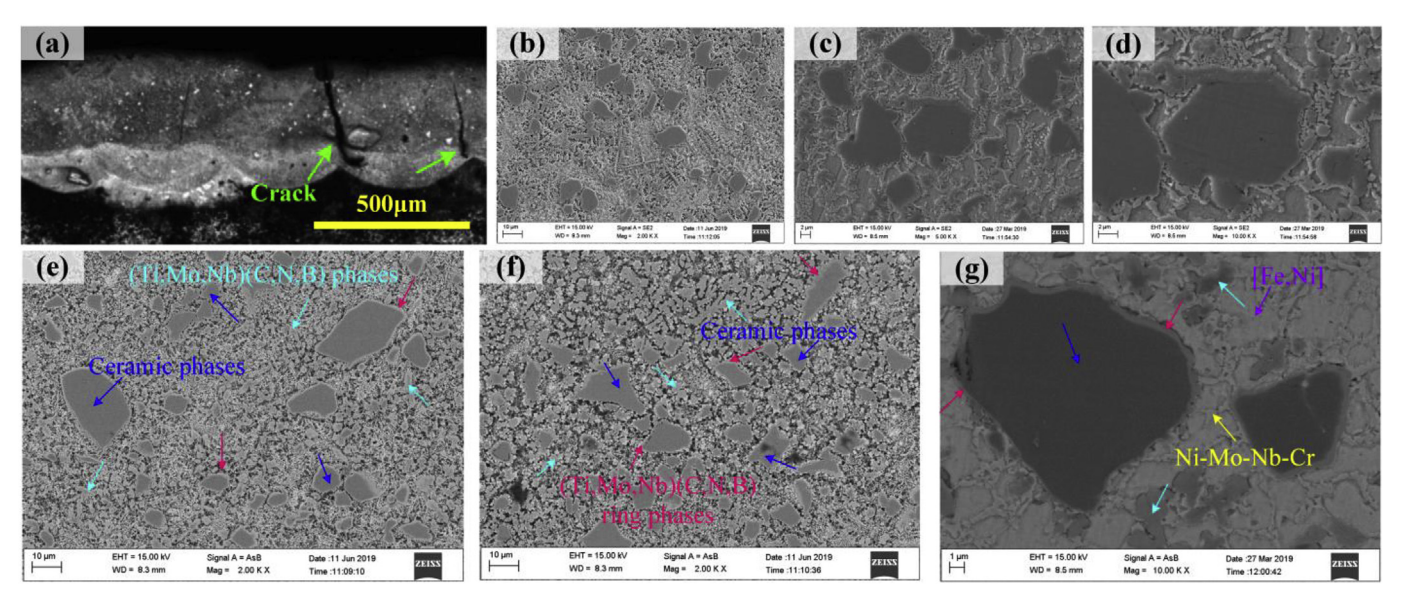


Fig. 11. Microstructure of sample 1. (a) Microscopic topography; (b)-(d) SEM images at different magnification; (e)-(b) BSE images at different magnification.

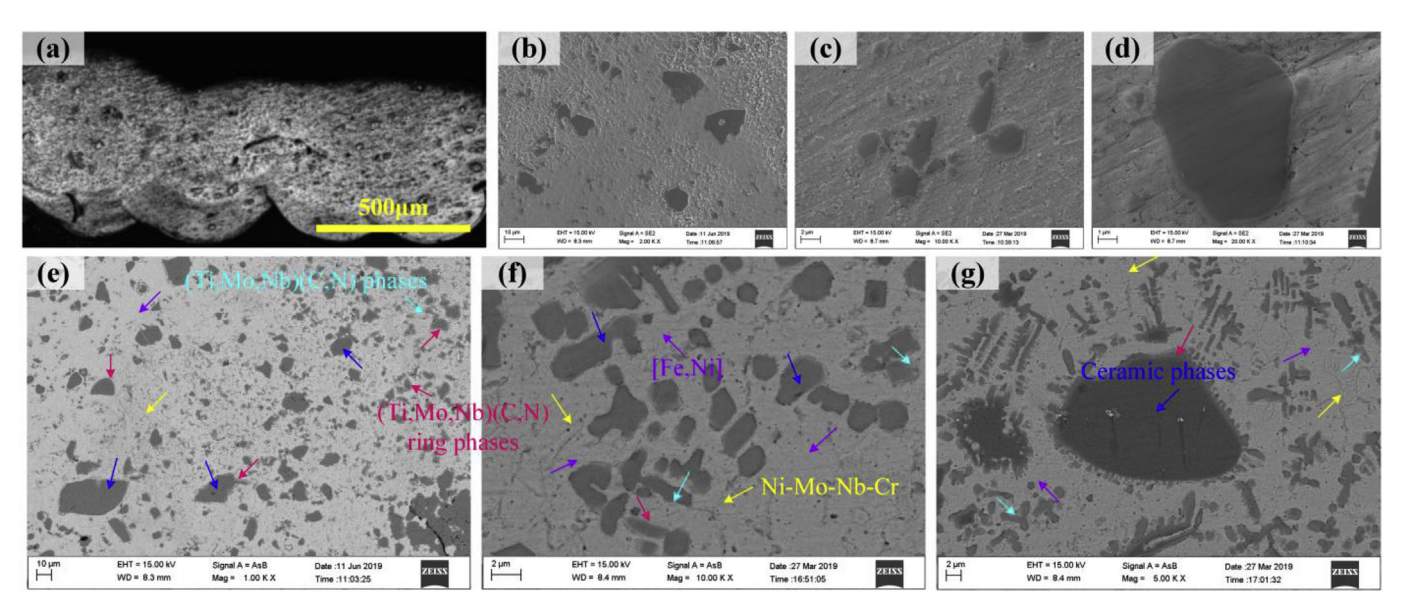


Fig. 12. Microstructure of sample 2. (a) Microscopic topography; (b)-(d) SEM images at different magnification; (e)-(b) BSE images at different magnification.

phase is the TiN ceramic phase, and the small particle phase around TiN phase is primarily a Ti–Mo–Nb solid solution. TiN has good wettability with the matrix, and a light gray ring phase appears around the reinforcement phase. The light gray ring phase around TiN primarily contains Ti, N, C, Mo, and Nb, forming multiphase (Ti, Nb, Mo) (C, N). The dark gray-black phase in the lower right corner of Fig. 9(a) is the TiC ceramic phase. The TiC ceramic phase is darker than that of TiN phase. Fig. 9(g) shows EDS spectra from the enhanced phase with different shapes and sizes of the reinforcement phase. Spectra 1–3 indicates the presence of 46.16% Ti-53.84% C, 46.2% Ti- and 53.8% C, and 49.63% Ti- and 50.37% C. The EDS spectra and XRD results show that TiC ceramic phase is the reinforcement phase at points 1, 2, and 3 in Fig. 9(g). Mo prevents enrichment and coarsening of TiN particles. A (Ti, Nb, Mo) (C, N) ring phase formed around the TiN single-phase ceramic particles.

EDS spectra of different phases in the backscatter image in Fig. 10 were also gathered. One should note that detection of B and C with EDS is not particularly accurate. Table 4 shows the elemental content at points 1–4 in Fig. 10. The milky white phase in point 1 primarily contains Ti, C, Mo, and Nb, although B must exist in the coating because

 $10\%B_4C$ was added to the initial powder used for laser cladding. According to the XRD results in Fig. 3 and the results from sample 1, one can see that the milky white phase is (Ti, Mo, Nb) (B, C). At point 3, Ti, N, and C are the predominant elements, confirming the presence of the ceramic phase. The ring phase appears around the ceramic phase. Ti, C, Mo, Nb, Mo, and B may exist at point 2. The results from samples 1 and 2 show that the ring phase was (Ti, Mo, Nb) (B, C). Point 4 is an intracellular area of a grain, where the predominant elements are Fe, Ni and Cr, indicating the phase is an [Fe, Ni] solid solution.

3.1.3. Coating microstructure analysis

Figs. 11(a), 12(a) and 13(a) show the macro-morphology of samples 1, 2, and 4 respectively; the images in these figures were gathered using the laser confocal microscope. There were no obvious pores or cracks in samples 2 and 4, but obvious cracks appeared in the overlap area in sample 1. One can see that all coatings exhibit strong metallurgical bonding to the substrate. In some studies, porosity and cracks also form in coatings containing the B_4C ceramic phase [31,32]. The toughness of B_4C is poor and it cracks easily. The toughness of the composite coating can increase when TiC is added [22]. The content of B_4C in sample 1 is

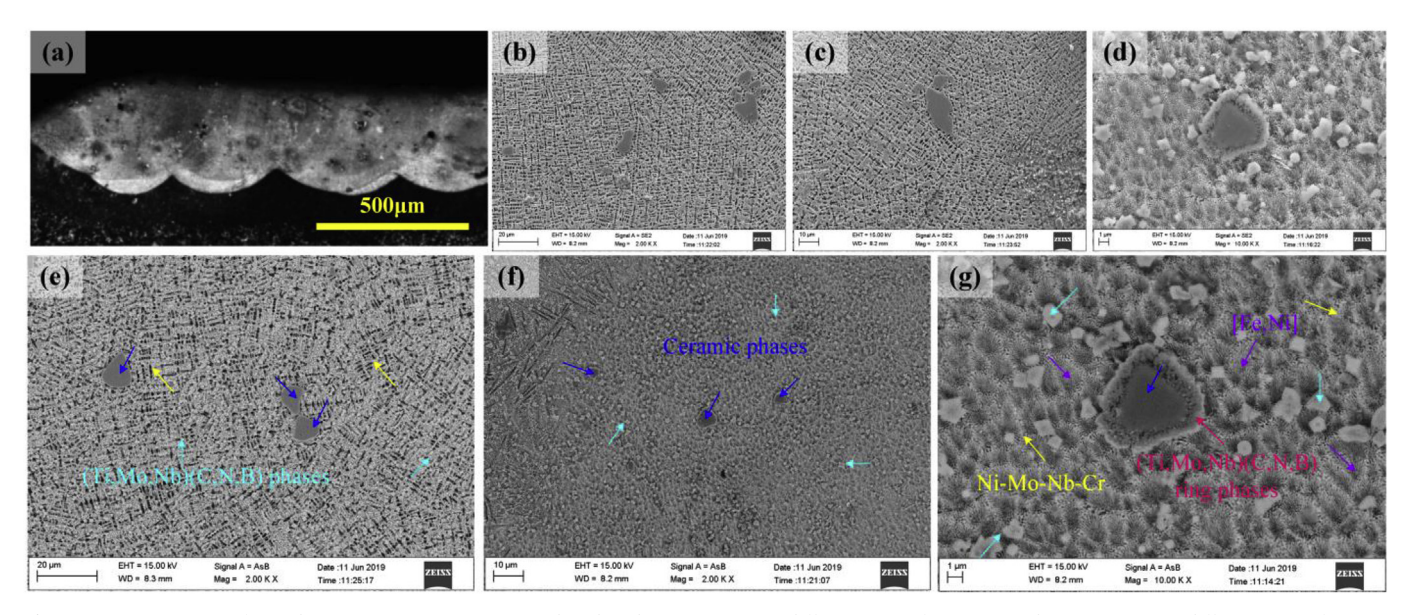


Fig. 13. Microstructure of sample 4. (a) Microscopic topography; (b)-(d) SEM images at different magnification; (e)-(b) BSE images at different magnification.

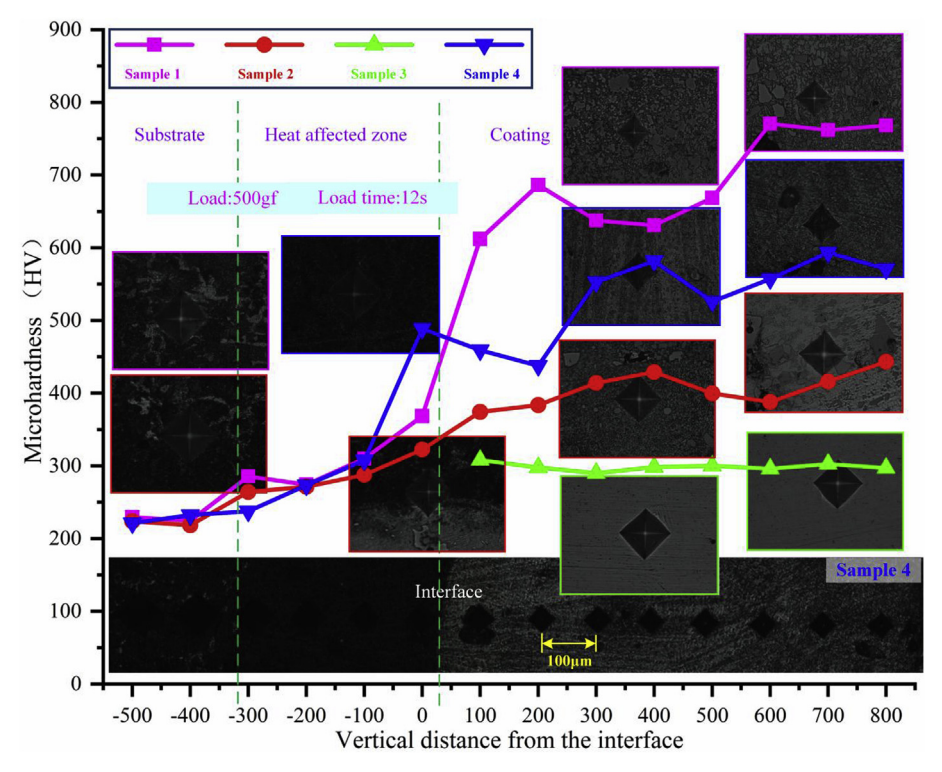


Fig. 14. Microhardness distribution along the depth of the cross section.

10%, and a small amount of gas is produced during cladding via decarbonization and oxidation. This gas cannot evaporate away to form pores, thus it forms the source of crack propagation instead. However, the low melting point phases formed by TiC, TiN and B_4C with Ni204 alloy in the coating may cause cracking. The content of B_4C in sample 4 is also 10%, but the content of the ceramic phase in the melt layer is low, and the concentration of the low melting point phase is not as high as that in sample 1, thus cracks do not form. The Ti(C, N) high melting point phase and multiphase (Ti, Nb, Mo) (C, N) primarily formed in sample 2, which has similar properties as TiN and TiC particles. Therefore, the crack size in sample 2 is smaller than that in sample 1.

Fig. 11(b)-(d), 12(b)-(d), and 13(b)-(d) show SEM images from samples 1, 2, and 4 at different magnifications, respectively. Grain

refinement is the most obvious of sample 1, followed by samples 4 and 2. When TiN and TiC were added to sample 2, the Ti(C, N) phase was easily in situ synthesized during laser cladding. TiN and TiC clustered in the coating, and the nucleation rate in the coatings was non-uniform. However, when B₄C was added to samples 1 and 4, the grain size was obviously refined, and TiC and TiN do not predominantly form Ti(C, N). Some B₄C particles are dispersed in the coating, and some of these particles react with TiC to form carbides and nitrides such as TiB₂, TiBN and Ni₄B₃. The ceramic phases do not aggregate in the coating, and the hard phase becomes more uniform. Therefore, the nucleation rate in the coating is more uniform, and grain refinement is obvious.

Fig. 11(e)-(g), 12(e)-(g), and 13(e)-(g) show BSE images from samples 1, 2, and 4 at different magnifications, respectively. The

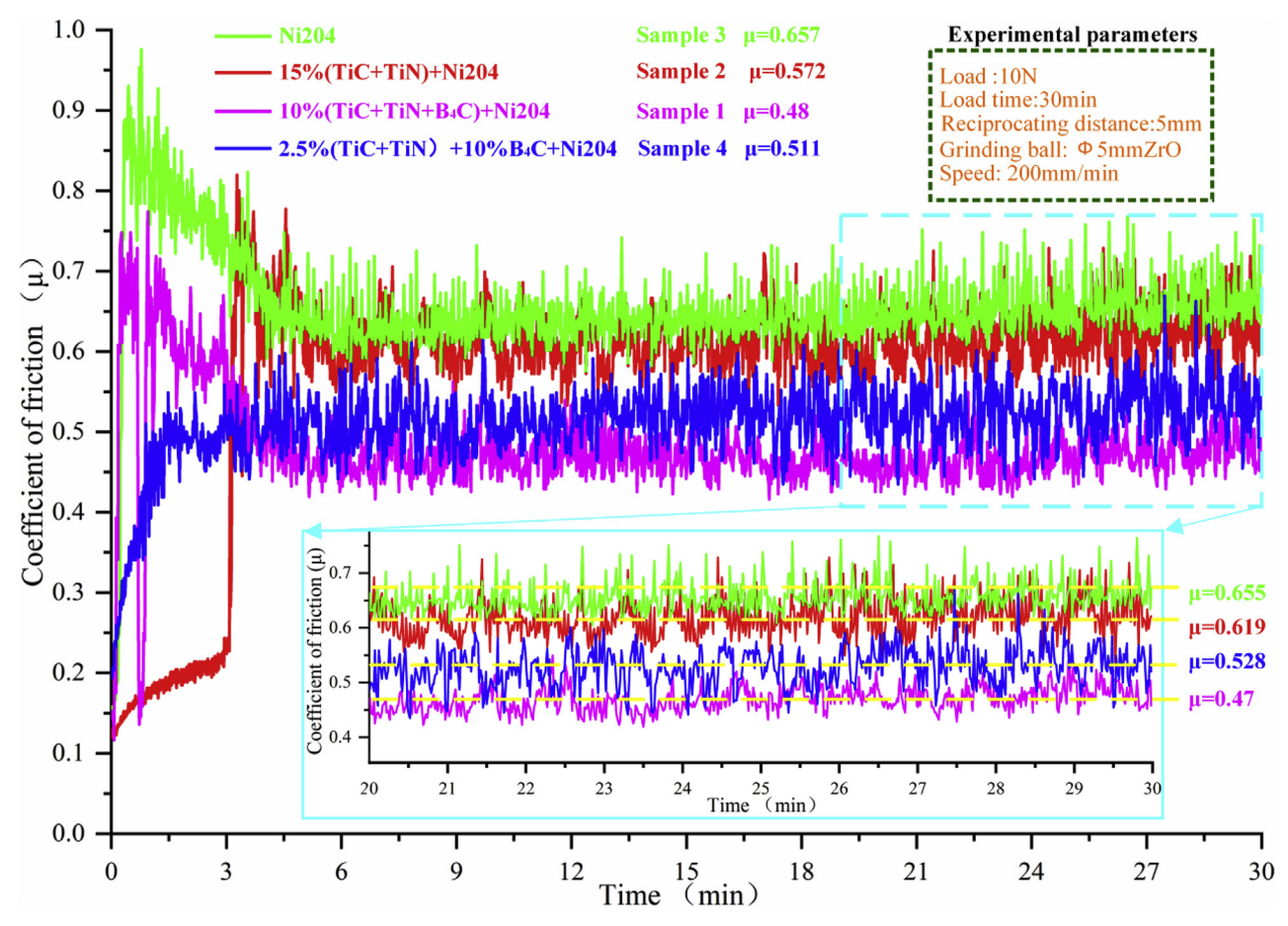


Fig. 15. Friction coefficient curves.

distribution of Ti(C, N), TiC, and TiN ceramic phases in sample 2 is less homogeneous and has serious enrichment. The distribution of the reinforced phase is uniform in samples 1 and 4. The grain boundary along all coatings is primarily Ni–Cr–Mo–Nb, while the intragranular is primarily [Fe, Ni]. Within samples 1 and 4, the (Ti, Nb, Mo) (C, N, B) ring phases primarily appeared around the ceramic phases (TiN, TiC, Ti(C, N)). Meanwhile, the (Ti, Nb, Mo) (C, N) ring phases primarily appeared around the ceramics phases (TiN, TiC) in sample 2. Multiphase (Ti, Nb, Mo) (C, N, B) and (Ti, Nb, Mo) (C, N) appeared in samples 1 and 4, as well as sample 2, respectively.

3.2. Microhardness and friction coefficient

3.2.1. Microhardness of composite coating

Fig. 14 shows that the microhardness of the Ni-based coatings strengthened with different content of TiC, TiN, B_4C powders distributed along the depth direction. The results show that the microhardness of the coatings changes obviously. Sample 1 exhibits highest microhardness, followed by samples 4, 2, and 3. When 10% TiC + TiN + B4C was added, the microhardness of sample 1 was the highest and with an average value of $766.8 HV_{0.5}$. The addition of B_4C increased the content of borides and carbides in the coating, resulting in formation of a large number of multiphase (Ti, Mo, Nb) (C, N, B) and ceramic phases. The addition of B_4C also made the distribution of reinforced phase more uniform, which refined the grains. The uniform distribution of the reinforcement phase is responsible for the increased deformation resistance. Thus, the coating with B_4C has higher microhardness. The microhardness of samples 1, 2, and 4 were factors 2.6, 1.4, and 1.9 larger than that of sample 3, respectively.

3.2.2. Friction coefficient of the composite coating

Fig. 15 shows the friction coefficients over time from the Ni-based coatings strengthened with different content of TiC, TiN, and B_4C ceramic particles. The results show that the friction coefficient of the Ni204 coating is effectively improved by adding B_4C ceramics. The friction coefficient was unstable in the initial stage, but it tends to stabilize after some time. In this experiment, the average friction coefficient over 20–30 min was taken as the absolute friction coefficient for each sample. Sample 1 had the lowest friction coefficient, followed by sample 4, 2, and 3. Sample 1 exhibits a minimum friction coefficient of 0.47, which is a factor 1.393 smaller than that of sample 3 (Ni204-based coating). The original wear mechanism change when TiC, TiN and B_4C ceramic particles were added to the coating. When the grinding ball meets the ceramic phase, it prevents the small wear debris from forming during the wear process, thus reducing the friction coefficient [16,21].

The 2D and 3D wear morphologies of each specimen are shown in Fig. 16. In addition, the friction coefficient of the specimens was analyzed by combining 2D and 3D morphologies. The Ni2O4 coating contains deep furrow scratches, and material was removed uniformly. One can infer that abrasive wear occurs. As shown in Fig. 16(a) and (a1), the wear resistance is poor. When the ceramic phase was added, plough groove scratches were effectively improved. Fig. 16(b)-(d) and (b1)-(d1) show that the surface of the sample contains a shallow plough groove scratch. When the ceramic phase is encountered, the scratch is not obvious and even disappears. During cladding, the ceramic phases agglomerate in sample 2, and the distribution of ceramic phases was non-uniform. There are many large TiN particles in the coating that were not completely dissolved and agglomerated; these particles cannot completely react with TiC during cladding. However, the elemental

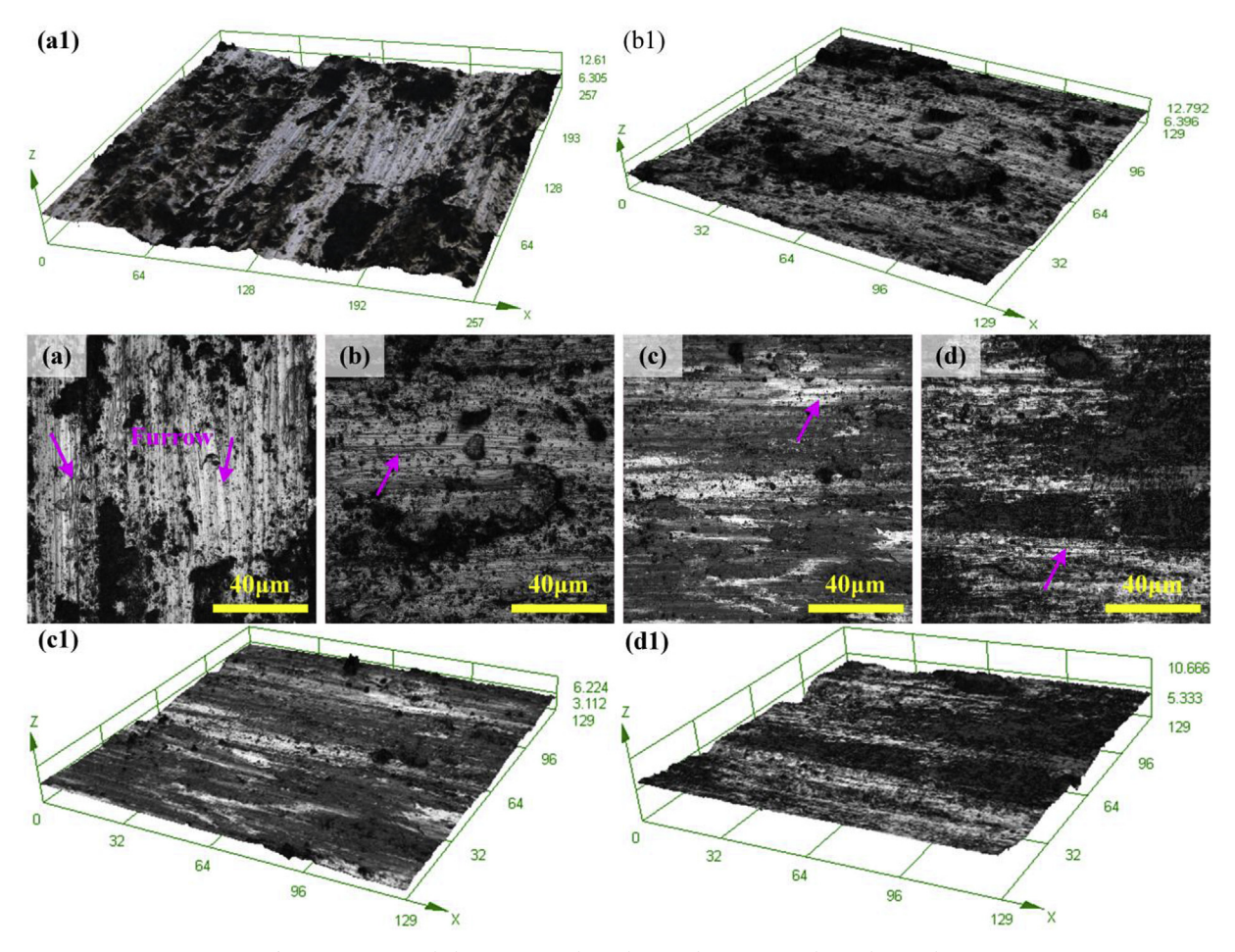


Fig. 16. Wear morphology. (a) Sample 3; (b) Sample 2; (c) Sample 1; (d) Sample 4.

distribution between Ti(C, N) phase and the Ni204 matrix is abrupt, and there is no ring phase around it. Bonding between the Ti (C, N) phase and the matrix is not as strong as that between samples 1 and 4. Therefore, it is not obvious how adding TiC and TiN increased the hardness and microhardness of the coatings [21]. Thus, the effect on the wear resistance was not obvious. When B₄C was added to the TiC/TiN/ Ni204 composite powder, the reaction between B₄C and TiC/TiN/ Ni204 composite powder was promoted. B₄C has high hardness and low friction coefficient. Although B₄C participates in the reaction and produces some low hardness and friction coefficient phases during cladding. However, ${\rm TiB_2}$ produced in the coating improves the compactness of B₄C [33], and B₄C disperses in the coating which benefits the coating property. The ring phase (Ti, Mo, Nb) (C, B, N) formed around the ceramic particles and multiphase (Ti, Mo, Nb) (C, B, N) increased the wettability of the ceramic phase and matrix. The newly formed carbides and nitrides in the coatings improved the friction coefficient of the coatings. The size of the reinforcing phase in the coating decreased and the distribution became uniform. Solid solution strengthening, dispersion strengthening, and fine grain strengthening occurred when B₄C was added to the coating, effectively increasing the coating's friction coefficient. The wear surface on all samples became smoother. The reinforcing phase in the coating terminates abrasive wear of the initial coating. The abrasive is rubbed repeatedly during the reciprocating wear process, which gradually changes the original wear mechanism to adhesive wear, thus improving the smoothness of the surface [21].

4. Conclusion

In this study, TiC-TiN-B4C composite ceramic coatings were

prepared on 45 steel by laser cladding. The effect of TiC, TiN, Ti(C, N) and (Ti, Mo, Nb) (C, B, N) ceramic phases in the microstructure on microhardness and friction coefficient was studied.

The composite coatings included TiC, TiN, Ti (C, N) and Ni–Cr–Mo–Nb phases. TiC, Ti(C, N), and TiN ceramics had similar color, but the color of TiN is lighter than that of TiC. When TiC and TiN ceramic particles were added to the initial powder, (Ti, Mo, Nb) (C, N) ring phases, and (Ti, Mo, Nb), and (Mo, Nb) solid solutions appeared around the TiC, Ti(C, N), TiN ceramic phases. The appearance of the ring phase around the ceramic phase improves its wettability with the matrix. Adding B_4C promoted the reaction between the ceramic particles and the initial powder. As a result, the (Ti, Mo, Nb) (C, B, N) ring phase, and multiphase (Ti, Mo, Nb) (C, B, N) appeared in the coating, which effectively improved the performance of the coating.

The presence of the ceramic phase can increase the microhardness of the Ni204 coating. Composite ceramics with additional 10%TiC/10%TiN/10%B₄C exhibited microhardness that was a factor 1.8 larger than the coating with 15%TiC/15%TiN. The composite ceramic with 10%TiC/10%TiN/10%B₄C exhibited the largest microhardness with 766.8HV_{0.5}, which is a factor 2.6 higher than that of the initial Ni204 coating. The addition of B₄C promotes the formation of multiphase (Ti, Mo, Nb) (C, B, N) in the coating, as well as the (Ti, Mo, Nb) (C, B, N) ring phase around the Ti (N, C) ceramic phase, which increases the microhardness and decreases friction coefficient of the coating.

The coating with 10 wt% TiC, TiN and $B_4\text{C}$ exhibited the lowest friction coefficient, which is a factor 1.393 lower than that of the initial Ni204 coating. The multicomponent ceramic phase, carbides and nitrides formed after adding $B_4\text{C}$ in the coating changed the wear mechanism of the coating, made the wear surface smoother, and made the

wear marks shallower. In addition, the presence of the strengthening phase resists micro-cutting damage caused by hard spot on the cladding layer.

Acknowledgement

This work was support by the Fundamental Research Funds for the Central Universities (N180306004); the Ministry of Industry and Information Technology of China under Grant (No. 201675514); and the Science and Technology Planning Project of Shenyang under Grant (No.18006001).

Appendix A. Supplementary data

Supplementary data to this article can be found online at https://doi.org/10.1016/j.ceramint.2019.07.070.

References

- Z. Feng, M. Tang, Y. Liu, Z. Yan, G. Li, In situ synthesis of TiC-TiN-reinforced Febase plasma cladding coatings, Surf. Eng. 34 (4) (2018) 309–315, https://doi.org/ 10.1080/02670844.2017.1349362.
- [2] M.Q. Wan, J. Shi, L. Lei, Z.Y. Cui, H.L. Wang, X. Wang, A Comparative study of the microstructure, mechanical properties and corrosion resistance of Ni- or Fe-based composite coatings by laser cladding, J. Mater. Eng. Perform. 27 (2018) 2844–2854, https://doi.org/10.1007/s11665-018-3282-1.
- [3] Y. Cai, Y. Chen, Z. Luo, F. Gao, L. Li, Manufacturing of FeCoCrNiCux mediumentropy alloy coating using laser cladding technology, Mater. Des. 133 (2017) 91–108, https://doi.org/10.1016/j.matdes.2017.07.045.
- [4] Z. Ban, L.L. Shaw, Characterization of thermal sprayed nanostructured WC-Co coatings derived from nanocrystalline WC-18wt. %Co powders, J. Therm. Spray Technol. 12 (2003) 112–119, https://doi.org/10.1361/105996303770348564.
- [5] N. Wei, H.C. Jie, W. Jun, G.W.C. Jiang, Effects of forming conditions and TiC-TiB₂ contents on the microstructures of self-propagating high-temperature synthesized NiAl-TiC-TiB₂ composites, Acta Metall. Sin. 28 (2015) 39–47, https://doi.org/10.1007/s40195-014-0163-y.
- [6] M. Wang, W. Wang, H. Chen, Y. Li, Understanding micro-diffusion bonding from the fabrication of B₄C/Ni composites, Int. J. Min. Met. Mater. 25 (2018) 365–374, https://doi.org/10.1007/s12613-018-1580-0.
- [7] C. Feng, V. Guipont, M. Jeandin, O. Amsellem, F. Pauchet, R. Saenger, S. Bucher, C. Iacob, B₄C/Ni composite coatings prepared by cold spray of blended or CVDcoated powders, J. Therm. Spray Technol. 21 (2012) 561–570, https://doi.org/10. 1007/s11666-012-9774-x.
- [8] M. Qunshuang, L. Yajiang, W. Juan, Int . Effects of Ti addition on microstructure homogenization and wear resistance of wide-band laser clad Ni60/WC composite coatings, Int. J. Refract. Met. H 64 (2017) 225–233, https://doi.org/10.1016/j. ijrmhm.2016.11.002.
- F. Wu, Effect of Mo on microstructures and wear properties of in situ synthesized Ti (C, N)/Ni-based composite coatings by laser cladding, Materials 10 (2017), https://doi.org/10.3390/ma10091047 104701-1047012.
- [10] D. Shu, Z. Li, K. Zhang, C. Yao, D. Li, Z. Dai, In situ synthesized high volume fraction WC reinforced Ni-based coating by laser cladding, Mater. Lett. 195 (2017) 178–181, https://doi.org/10.1016/j.matlet.2017.02.076.
- [11] L. Ma, J. Yu, X. Guo, Y. Zhang, H. Gong, Pressureless densification and properties of TiB₂-B₄C composite ceramics with Ni as additives, Micro & Nano Lett. 13 (2018) 947-950, https://doi.org/10.1049/mnl.2017.0709.
- [12] Z. Li, M. Wei, K. Xiao, Z. Bai, W. Xue, C. Dong, D. Wei, Microhardness and wear resistance of Al₂O₃-TiB₂-TiC ceramic coatings on carbon steel fabricated by laser cladding, Ceram. Int. 45 (2019) 115–121, https://doi.org/10.1016/j.ceramint. 2018 09 140
- [13] A. You, M.A.Y. Be, Optimization of laser cladding of cold spray coatings with B₄C

- and Ni powders, AIP Conf. Proc. 020054 (2017) 1–5, https://doi.org/10.1063/1.
- [14] Y. Li, P. Zhang, P. Bai, L. Wu, B. Liu, Z. Zhao, Microstructure and properties of Ti/ TiBCN coating on 7075 aluminum alloy by laser cladding, Surf. Coating. Technol. 334 (2018) 142–149, https://doi.org/10.1016/j.surfcoat.2017.11.034.
- [15] Q. Lin, R. Sui, Wetting of carbide ceramics (B₄C, SiC, TiC and ZrC) by molten Ni at 1753K, J. Alloy. Comp. 649 (2015) 505–514, https://doi.org/10.1016/j.jallcom. 2015.07.138.
- [16] Y. Lyu, Y. Sun, F. Jing, On the microstructure and wear resistance of Fe-based composite coatings processed by plasma cladding with B₄C injection, Ceram. Int. 41 (2015) 10934–10939, https://doi.org/10.1016/j.ceramint.2015.05.036.
- [17] T. Bodziony, S.M. Kaczmarek, A. Biedunkiewicz, G. Leniec, P. Figiel, Magnetic study of nanocrystalline TiB₂, TiC, B₄C powders doped to AISI 316L austenitic steel, Acta Phys. Pol., A 132 (2017) 62–67, https://doi.org/10.12693/APhysPolA.132.62.
- [18] W. Min-min, J. Bo, Z. Feng, The effect of reinforcements on superplasticity of in situ synthesized (TiB+TiC)/Ti matrix composite, Acta Mater. 54 (2006) 1955–1959, https://doi.org/10.1016/j.scriptamat.2006.01.044.
- [19] M. Processing, Electrodeposition and hardness and corrosion resistance propertie of Ni/nano-B₄C composite coatings, Adv. Mater. (2012) 2055–2060 https://org.doi/ 10.4028/www.scientific.net/AMR.399-401.2055.
- [20] C.L. Yeh, C.Y. Ke, Y.C. Chen, In situ formation of TiB₂/TiC and TiB₂/TiN reinforced NiAl by self-propagating combustion synthesis, Vacuum 151 (2018) 185–188, https://doi.org/10.1016/j.vacuum.2018.02.024.
- [21] L. Yang, T. Yu, M. Li, Y. Zhao, J. Sun, Microstructure and wear resistance of in-situ synthesized Ti (C, N) ceramic reinforced Fe-based coating by laser cladding, Ceram. Int. (2018) 1–11, https://doi.org/10.1016/j.ceramint.2018.09.025.
- [22] J. Sun, C. Liu, R. Wang, Low pressure hot pressing of B4C matrix ceramic composites improved by Al2O3 and TiC additives, Mater. Sci. Eng., A 519 (2009) 27–31, https://doi.org/10.1016/j.msea.2009.06.016.
- [23] J.L. Sun, Development of New B4C Composite Ceramic Nozzle and Study on its Erosion Mechanisms, Doctoral Dissertation Shandong University, China, 2017.
- [24] X. Wang, H. Shun, C. Li, X. Wang, D. Sun, The performances of TiB2-contained iron-based coatings at high temperature, Surf. Coating. Technol. 201 (2006) 2500–2504, https://doi.org/10.1016/j.surfcoat.2006.04.025.
- [25] E. Conforto, D. Mari, T. Cutard, The role of molybdenum in the hard-phase grains of (Ti, Mo)(C, N)–Co cermets, Philos. Mag. A 6435 (2006), https://doi.org/10.1080/ 14786430310001659516.
- [26] G. Dong, J. Xiong, M. Yang, Z. Guo, W. Wan, Effect of Mo 2 C on erosion corrosion resistance behavior of Ti(C, N)-based cermets, Wear 294–295 (2012) 364–369, https://doi.org/10.1016/j.wear.2012.05.013.
- Y. Li, N. Liu, Effect of Mo addition on the microstructure and mechanical properties of ultra-fine grade TiC-TiN-WC-Mo₂C-Co cermets, Int. J. Refract. Met. H 26 (2008) 190–196, https://doi.org/10.1016/j.ijrmhm.2007.05.005.
 J.H. Jang, Y. Heo, C. Lee, H.K.D.H. Bhadeshia, D. Suh, Interphase precipitation in
- [28] J.H. Jang, Y. Heo, C. Lee, H.K.D.H. Bhadeshia, D. Suh, Interphase precipitation in Ti–Nb and Ti–Nb–Mo bearing steel Interphase precipitation in Ti–Nb and Ti–Nb–Mo bearing steel, Mater. Sci. Technol. 29 (3) (2014) 309–313, https://doi.org/10. 1179/1743284712Y.0000000131.
- [29] X. He, X. Zhang, Y. Li, J. Huang, Effect of Mo on microstructure and mechanical properties of Nb-Ti-C-B multiphase alloy, J. Alloy. Comp. 551 (2013) 578–583, https://doi.org/10.1016/j.jallcom.2012.11.052.
- [30] X. Zhang, X. He, C. Fan, Y. Li, G. Song, Microstructural and mechanical characterization of multiphase Nb-based composites from Nb-Ti-C-B system, Int. J. Refract. Metals Hard Mater. 41 (2013) 185–190, https://doi.org/10.1016/j.ijrmhm. 2013.03.010.
- [31] A. Moradkhani, H. Baharvandi, M. Mahdi, M. Samani, Mechanical properties and microstructure of B4C–NanoTiB2–Fe/Ni composites under different sintering temperatures, Mater. Sci. Eng., A 665 (2016) 141–153, https://doi.org/10.1016/j. msea.2016.04.034.
- [32] M. Mashhadi, E. Taheri-nassaj, M. Mashhadi, V.M. Sglavo, Pressureless sintering of B4C-TiB2 composites with Al additions, Ceram. Int. 37 (2011) 3229–3235, https://doi.org/10.1016/j.ceramint.2011.05.096.
- [33] C. Xu, Y. Cai, K. Flodström, Z. Li, S. Esmaeilzadeh, G. Zhang, Spark plasma sintering of B4C ceramics: the effects of milling medium and TiB2 addition, Int. J. Refract. Metals Hard Mater. 30 (2012) 139–144, https://doi.org/10.1016/j.ijrmhm.2011. 07.016.